AGU PUBLICATIONS

JGR

Journal of Geophysical Research: Oceans

RESEARCH ARTICLE

10.1002/2017JC013394

On the Decrease of the Oceanic Drag Coefficient in High Winds

Mark A. Donelan[1]

[1]Rosenstiel School of Marine and Atmospheric Science, University of Miami, Miami, FL, USA

Key Points:

- The sheltering coefficient (in the formulation of wave drag) is strongly Reynolds number dependent
- The decreasing drag coefficient in high winds is caused by the sharp fall-off of the sheltering coefficient
- Rapid intensification of hurricanes is explained by the Reynolds number dependency of the sheltering coefficient

Supporting Information:

- Supporting Information S1
- Data Set S1
- Data Set S2
- Data Set S3
- Data Set S4
- Data Set S5
- Data Set S6
- Data Set S7
- Data Set S8
- Data Set S9
- Data Set S10
- Data Set S11
- Data Set S12
- Data Set S13
- Data Set S14
- Data Set S15
- Data Set S16
- Data Set S17
- Data Set S18

Correspondence to:
M. Donelan,
mdonelan@rsmas.miami.edu

Citation:
Donelan, M. A. (2018). On the decrease of the oceanic drag coefficient in high winds. *Journal of Geophysical Research: Oceans*, *123*. https://doi.org/10.1002/2017JC013394

Received 28 AUG 2017
Accepted 30 JAN 2018
Accepted article online 5 FEB 2018

Abstract The sheltering coefficient – prefixing Jeffreys' concept of the exponential wave growth rate at a gas-liquid interface – is shown to be Reynolds number dependent from laboratory measurements of waves and Reynolds stresses. There are two turbulent flow regimes: wind speed range of 2.5 to 30 m/s where the drag coefficients increase with wind speed, and wind speed range of 30 to 50 m/s where sheltering/drag coefficients decrease/saturate with wind speed. By comparing model calculations of drag coefficients – using a fixed sheltering coefficient – with ocean observations over a wind speed range of 1 to 50 m/s a similar Reynolds number dependence of the oceanic sheltering coefficient is revealed. In consequence the drag coefficient is a function of Reynolds number and wave age, and not just wind speed as frequently assumed. The resulting decreasing drag coefficient above 30 m/s is shown to be critical in explaining the rapid intensification so prominent in the climatology of Atlantic hurricanes. The Reynolds number dependence of the sheltering coefficient, when employed in coupled models, should lead to significant improvements in the prediction of intensification and decay of tropical cyclones. A calculation of curvature at the wave crest suggests that at wind speeds above 56.15 m/s all waves––breaking or not––induce steady flow separation leading to a minimum in the drag coefficient. This is further evidence of the veracity of the observations of the oceanic drag coefficient at high winds.

1. Introduction

Measurements of the tangential stress, τ exerted by flowing air (wind) on a water surface have revealed that there are at least 3 regimes in the drag coefficient $(Cd=\tau/\rho_a U_{10}^2)$ versus wind speed at 10 m height, U_{10}; ρ_a is the air density. The readily measurable quantity – the total stress – consists of two parts: skin stress and form stress, which have the same meaning as those applied to a solid body immersed in a fluid stream. The slopes of the waves on the surface add form stress and reduce the skin stress through sheltering of the surface downstream of steep crests (Reul, 1998). No waves are formed at wind speeds less than about 2.5 m/s (Donelan & Pierson, 1987), and the first regime ($0 < U_{10} < 2.5$ m/s) of strictly skin stress has the well-known inverse dependence of Cd on U_{10}, characteristic of viscous boundary layers. Above U_{10} of 2.5 m/s until about 30 m/s the waves grow, and with them the form stress, leading to a general increase of Cd with U_{10}: Donelan et al. (2004) Laboratory; Edson et al. (2013) Ocean. The high wind regime ($30 < U_{10} < 60$ m/s) is characterized by a saturated drag coefficient in the laboratory (Donelan et al., 2004; Takagaki et al., 2012), and a decreasing Cd on the ocean (Holthuijsen et al., 2012; Jarosz et al., 2007; Powell et al., 2003).

Since the publication of papers showing field observations of decreasing drag coefficients in high winds (Powell et al. 2003) and laboratory measurements of constant drag coefficients in high winds (Donelan et al. 2004), several attempts have been made to explain these dissimilar, but probably related, phenomena. Makin (2005) suggests that, in high winds, sea-spray droplets form a stable layer near the surface, which damps the turbulence and so reduces the drag coefficient. Kudryavtsev and Makin (2007) and Kukulka et al. (2007) both consider the sheltering of short waves due to air-flow separation from the crests of breaking longer waves; neither can explain the decreasing drag coefficients in high winds. Troitskaya et al. (2012) examine, theoretically and experimentally, the laboratory saturation of the drag coefficient at wind speeds exceeding 25 m/s. They suggest that the tearing of the steep crests reduces the slopes of the surface and hence the aerodynamic roughness. Their quasi-linear theory of wind-wave generation does not admit decreasing drag coefficients in high winds. Soloviev et al. (2014) explored the generation of spume by the Kelvin-Helmholtz shear instability producing a thin foam layer that suppresses the short capillary-gravity waves and reduces the drag coefficient. Golbraikh and Shtemler (2016) contend that the aerodynamic roughness length of the surface can be treated as the sum of roughness lengths of the foam-covered and the foam-free parts of the surface. Satellite measures of foam coverage yield a decreasing drag coefficient at high winds. Takagaki et al. (2016), in a laboratory experiment, identify the flattening of the dominant waves as the cause of saturation of the drag coefficient at high wind speeds.

These studies explore various physical effects that may alter the aerodynamic characteristics of the air-sea interface, but they do not provide a simple prescription that may be used in a fully coupled (atmosphere-wave-ocean) hurricane prediction model. For the mechanical coupling of air and sea, a set of parametric relations between the drag coefficient components (skin and form) and suitable dimensionless ratios of wind and wave variables is needed. This paper is devoted to finding such a set.

With increasing wind, the boundary layer flow over water waves transitions from laminar to turbulent to fully separated. Such flows, involving a balance between viscous and inertia forces, are Reynolds number dependent. Thus one might expect a similarity in Reynolds number behaviour of the sheltering coefficient on increasing wave heights and the form drag coefficient on a solid cylinder of fixed diameter. The smooth flow regime is well understood so we consider here the turbulent regimes: $U_{10} > 2.5$ m/s.

The key to understanding regimes 2 and 3 lies in the realization that the sheltering coefficient of the form stress is Reynolds number dependent. In section 2, this dependence is revealed from laboratory data; section 3 deals with the corresponding dependence on the ocean; section 4 explores the expected intensification of hurricanes with high wind regimes of: a) constant drag coefficients, b) decreasing drag coefficients. The discussion in section 5 lays down a generalized wind-wave coupling for use in coupled atmosphere-wave-ocean models.

2. The Sheltering Coefficient in the Laboratory

Wind-wave coupling generally follows the ideas of Jeffreys (1924, 1925) or Miles (1957), both couched in terms of the energy input to the waves. Jeffreys's concept of the wave energy input from the wind, S_{in} (Donelan et al., 2012) is adapted here to include all wind-generated waves: gravity, capillary-gravity and capillary:

$$S_{in}=A_1((U_{\pi/k}-u_{-1/k})\cos\theta-c(k))|(U_{\pi/k}-u_{-1/k})\cos\theta-c(k)|\frac{\omega}{c^2(k)}\frac{\rho_a}{\rho_w}E(k,\phi) \tag{1}$$

where θ is the angle between wind direction and waves of wavenumber, k and direction, ϕ; $U_{\pi/k}$ is the wind speed at one half wavelength height; $u_{-1/k}$ is the wind-drift current at depth $1/k$ and c is the phase velocity; ω is the radian frequency of a wave and ρ_w is the water density. $E(k,\phi)$ is the variance (of surface elevation) spectrum defined such that variance, $\sigma^2=\int\int E(k,\phi)kdkd\phi$ and A_1 is the sheltering coefficient, a measure of the degree of sheltering of the surface downstream of a crest; $0 < A_1 < 1$.

The energy spectrum, $E'(k,\phi)$ is the variance spectrum times the water density and the effective mean downward vertical acceleration:

$$E'(k,\phi)=\rho_w\left(g+\frac{\gamma k^2}{\rho_w}\right)E(k,\phi) \tag{2}$$

where g is the gravitational acceleration and γ is the surface tension (N/m).

The drift current profile was estimated from the friction velocity, $u_*=U_{10}\sqrt{Cd}$ and the observation that, in a closed tank, the return drift begins at 13% of the depth of the tank (Donelan, 1978):

$$u_{-1/k}=\sqrt{\frac{\rho_a}{\rho_w}}\frac{u_*}{\kappa}\ln(0.13Dk) \tag{3}$$

where D is the depth of water in the tank (0.42 m) and κ is the von Karman constant = 0.4. The surface (−0.1 mm) drift from equation (3) is $0.55u_*$ as observed by Wu (1975) in a similar tank.

Large eddy simulations (Yang et al., 2013) leave no doubt that the Jeffreys concept of the sheltering of the troughs – due to flow separation at the crests – mimics the calculated growth rates for many experiments very well. This also supports the choice of wind speed for each wavenumber as the wind speed at a height of one half wavelength. There is however considerable variation of the sheltering coefficient among experiments. Indeed, direct measurements of the pressure near the surface in the laboratory (Donelan, 1999;

Grare et al., 2013) and the field (Donelan et al., 2006; Hsiao & Shemdin, 1983) yield sheltering coefficients between 0.1 and 0.5.

The high wind laboratory experiments of Donelan et al. (2004), which included measurements of wave spectra and total stress, provide an opportunity to determine the structure of the sheltering coefficient. The wind and wave data were sampled at 500 Hz and the wave data averaged to 50 Hz. Nine steady-state 10m equivalent wind speeds (between 8.95 and 40.5 m/s) are analyzed here. The measured wave spectra and their integral properties (significant height (cm), peak period (s), equilibrium range parameter, α and drag coefficient) are shown in Figures 1 and 2. They all indicate a regime change to quasi-saturation at about 30 m/s. (The equilibrium range parameter is defined by the spectrum (Donelan et al. 1985) converted to cyclic frequency, f from radian frequency: $\alpha = (2\pi)^4 g^{-2} f^5 \left(\frac{f}{f_p}\right)^{-1} F(f)$ in the range $1.5 < \frac{f}{f_p} < 4$). This experiment has been repeated by Takagaki et al. (2012) with the same results in the saturation of the drag coefficient and the integral wave parameters. The reduced growth of the spectrum beyond $U_{10} = 30$ m/s is evidently due to the small water depth – increasing bottom dissipation and limiting phase and group velocities. Nonetheless, the sheltering coefficient may be estimated by comparing the calculated form drag coefficient, Cd_{fc} to the measured form drag coefficient, Cd_{fm}.

The calculated form drag coefficient, Cd_{fc} may be obtained from (1) by noting that energy and momentum, M in progressive waves are connected via phase velocity: $E' = M \cdot c$, (Phillips, 1977)

$$Cd_{fc} = \rho_w \int_{-\pi}^{\pi} \int_{0}^{f_N} \left(g + \frac{\gamma k^2}{\rho_w} \right) \frac{S_{in}(f)}{c(f)} \cos\phi f df d\phi \, / \, \left(\rho_a \left((1-0.035) U_{10}\right)^2\right) \tag{4}$$

where $S_{in}(f)$ is (1) converted to frequency, f from wavenumber via the linear dispersion relation $\omega^2(k) = k\left(g + \frac{\gamma k^2}{\rho_w}\right) \tanh kD$, (Phillips, 1977); and the directional spreading function is taken from Donelan (2017); The reference velocity has been reduced by 3.5% to account for the surface wind drift (Wu, 1975). The sheltering coefficient, A_1 is set to 0.11.

The total stress was measured by hot-film anemometry at varying heights above the surface and evaluated at the surface via the vertical stress gradient equated to the downstream pressure gradient obtained from the pressure difference across two small ceiling holes 10m apart.

The measured form drag coefficient, Cd_{fm} is estimated by subtracting the sheltering-attenuated skin drag coefficient, Cd_s'; where, following Donelan et al. (2012), the attenuation factor varies from 1 (no form drag,

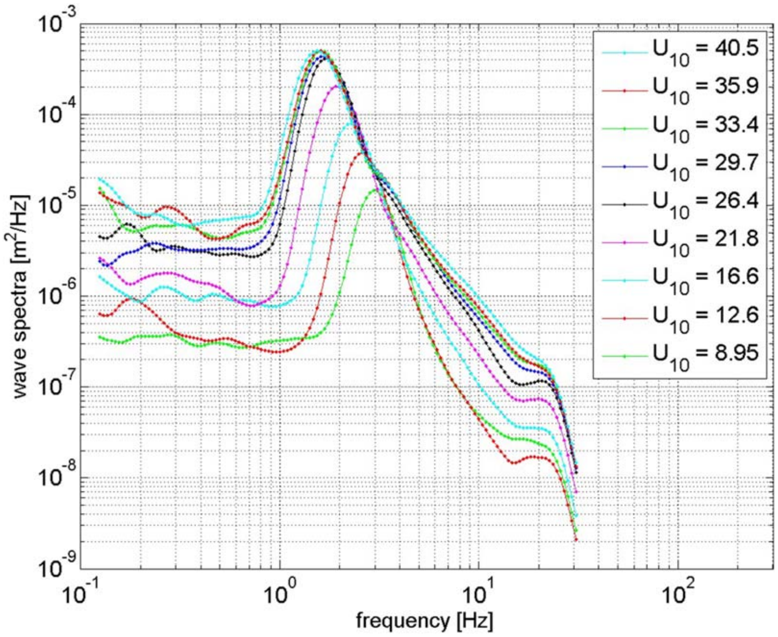

Figure 1. Measured laboratory wave spectra at various wind speeds and fetch of 14.3 m.

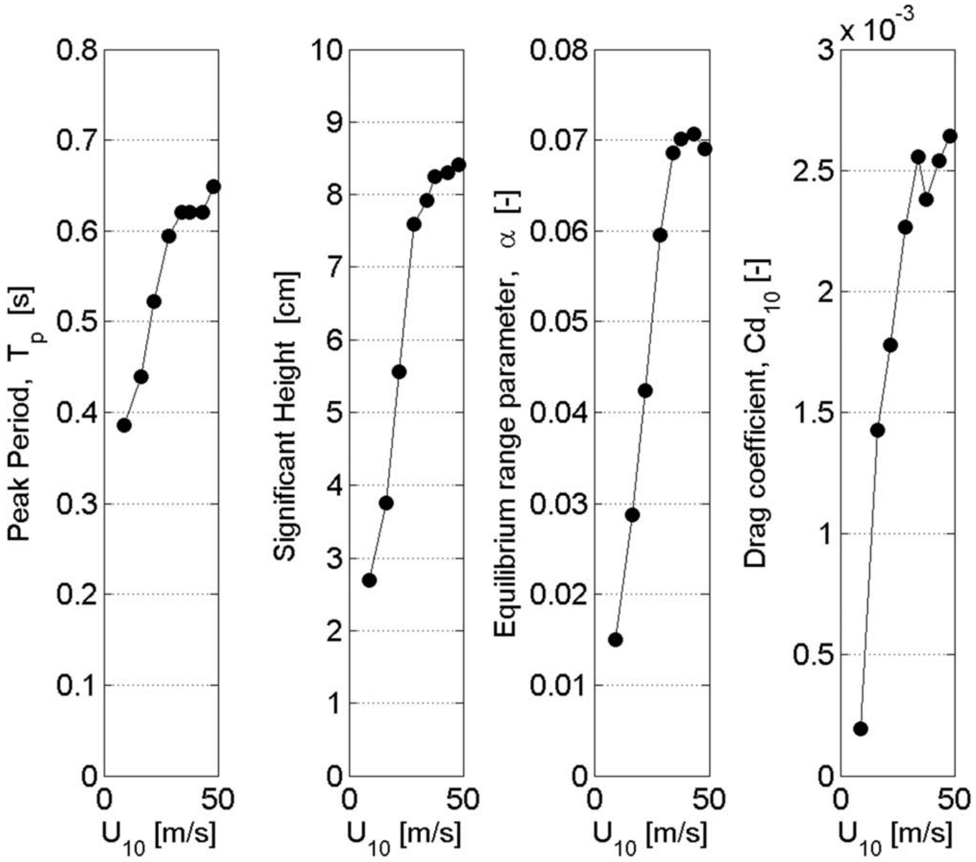

Figure 2. Integral properties of laboratory waves versus U_{10}. All properties show an abrupt change in slope at about 30 m/s.

no attenuation) to $\sim$0.5 (50% of surface area sheltered) as the form stress grows and more of the surface (skin) is sheltered and Cd_s attenuated accordingly:

$$Cd_{fm}=Cd-Cd_s'=Cd-\frac{Cd_s}{3}\left(1+\frac{2Cd_s}{Cd_s+Cd_{fm}}\right) \tag{5}$$

where Cd_s is the skin drag coefficient in the absence of form drag, due to the wind speed minus the 3.5% surface "wind drift." Equation (5) is solved iteratively with starting $Cd_{fm}=Cd/(1-0.035)^2$, i.e., corrected for wind drift of 3.5% of U_{10}. Thus the actual sheltering coefficient may be evaluated:

$$A_1=0.11\times Cd_{fm}/Cd_{fc} \tag{6}$$

This is graphed in Figure 3 versus the Reynolds number pertinent to the wind-wave generation process, Re_w:

$$\mathrm{Re}_w=\left(U_{\lambda_p/2}-c\left(\lambda_p\right)\right)\times Hs/\nu_a \tag{7}$$

where Hs is the measured significant height of the waves, ν_a is the kinematic viscosity of air and U and c are referenced to the wavelength of the spectral peak, λ_p, which is obtained from the measured peak frequency of the waves via the linear dispersion relation.

As expected the Reynolds number dependence of the sheltering coefficient is much like the drag coefficient on a circular cylinder normal to the flow (Batchelor, 1967, Figure 5.11.6). They both show 3 regimes as the Reynolds number increases: 1) decreasing as the laminar boundary layer thins; 2) constant as the turbulent boundary layer grows; 3) catastrophic decrease as the flow separates from the crests of the steepest waves, at that wind speed, or the diameter of the cylinder. In this last regime the growth of the waves compensates for the decrease of the sheltering coefficient – leading to a saturated drag coefficient above $U_{10} \sim 30$ m/s, as observed.

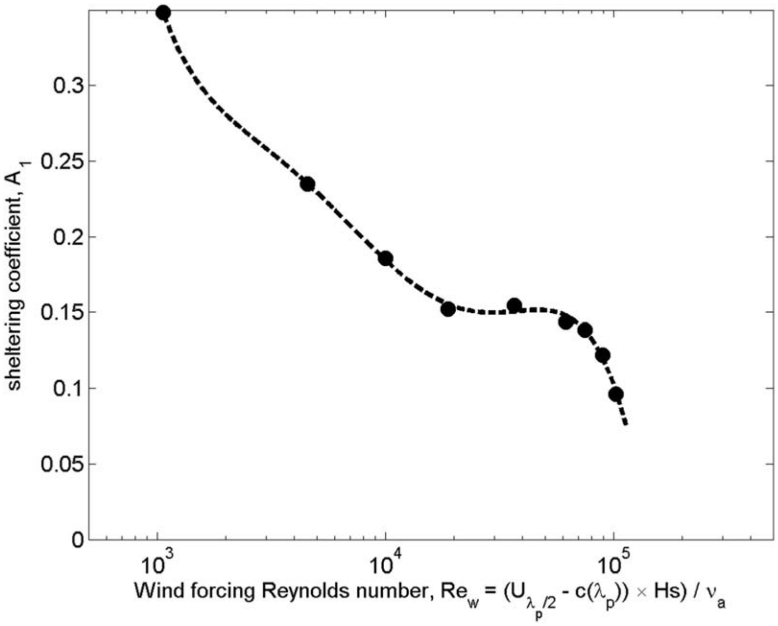

Figure 3. Sheltering coefficient versus Reynolds number from laboratory measurements (*Donelan et al*., 2004) with wind speeds, U_{10} from 8.95 to 40.5 m/s. Note the drop-off starting at 29.7 m/s (4^{th} highest Re_w).

3. The Sheltering Coefficient on the Ocean

The oceanic wind-wave coupling parameter, the sheltering coefficient, is also Reynolds number dependant and its dependency may be deduced by comparing measurements of the drag coefficients with drag coefficients modeled using a constant sheltering coefficient. The process is similar to the above (section 2) and requires reliable estimates of Cd over wind speeds of 1 to 50 m/s. The lower half of this range is well covered by the synthesis of many observations in 1 m/s bins from 1 to 23 m/s, "COARE 3.5" (Edson et al., 2013). For the upper half, the "bottom-up" measurements of Jarosz et al. (2007) provide guidance in the range of wind speeds of 20 to 50 m/s. These estimates, based on a momentum balance of currents beneath the passage of hurricane Ivan over the shelf of the northeastern Gulf of Mexico, refer to the stress delivered to the ocean and not the aerodynamic drag on the atmosphere. The former is less than the latter by the momentum advected away by the large waves. There is also uncertainty in the stress delivered to the bottom of the water column. There is, however, a region of overlap between the Edson et al. (2013) and Jarosz et al. (2007) measurements: 20 to 23 m/s. Consequently the Jarosz et al. (2007) drag coefficient estimates are increased by 0.0004 to bring them up to the Edson et al. (2013) estimates in the overlap region.

The combined observational evidence for the aerodynamic drag coefficient on the open ocean, Cd_o is plotted in Figure 4. For comparison with the calculated form drag, which was computed with respect to the wind drift, Cd_o is increased by $(1-0.035)^{-2} \approx 1.074$ corresponding to surface wind drift of 3.5% of wind speed (Wu, 1975). Similarly, Cd_s is the skin drag coefficient in the absence of form drag, due to the wind speed minus the 3.5% surface "wind drift". The observed form drag coefficient, Cd_{fo} is obtained (as in section 2) by solving equation (8) iteratively with starting $Cd_{fo}=1.074Cd_o$

$$Cd_{fo}=1.074Cd_o-\frac{Cd_s}{3}\left(1+\frac{2Cd_s}{Cd_s+Cd_{fo}}\right) \tag{8}$$

Cd_{fc}, the calculated drag coefficients with constant sheltering coefficient, $A_1=0.11$ is computed in the wave and wind stress model (UMWM – University of Miami Wave Model) expanded to include all waves – gravity, capillary-gravity and capillary – UMWM_wideband (see Appendix A):

$$Cd_{fc}=\rho_w\int_{-\pi}^{\pi}\int_{0}^{\infty}\left(g+\frac{\gamma k^2}{\rho_w}\right)\frac{S_{in}(k)}{c(k)}\cos\phi k dk d\phi \,/\, \left(\rho_a\left((1-0.035)U_{10}\right)^2\right) \tag{9}$$

3As before (section 2) Cd_{fc} is referred to the wind speed minus 3.5% surface wind drift. The corresponding total drag coefficients are also shown in Figure 4. Thus the actual sheltering coefficient may be evaluated:

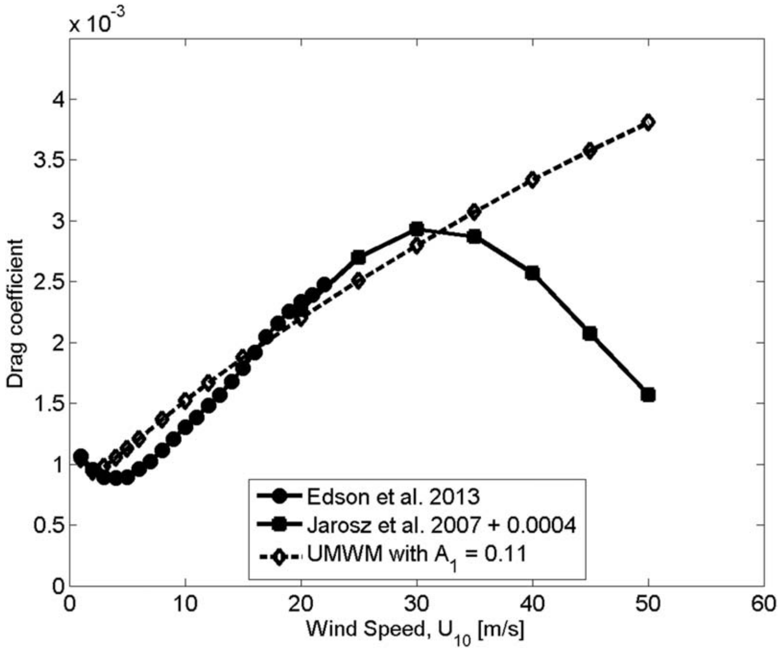

Figure 4. Observed and modeled (field) air-sea drag coefficients.

$$A_1(\mathrm{Re}_w)=0.11\times Cd_{fo}/Cd_{fc} \tag{10}$$

Here Re_w is calculated using the fetch-limited laws derived from Donelan et al. (1985):

$$T_p=0.54g^{-0.77}U_{10}^{0.54}X^{0.23} \tag{11}$$

$$Hs=4\times\sqrt{8.415\times10^{-7}g^{-1.241}U_{10}^{2.482}X^{0.759}} \tag{12}$$

where T_p is the period of the spectral peak and X is the fetch in meters. The resulting sheltering coefficients, for fetch of 230 km, are graphed versus the wind-forcing Reynolds number Re_w in Figure 5. Fetch of

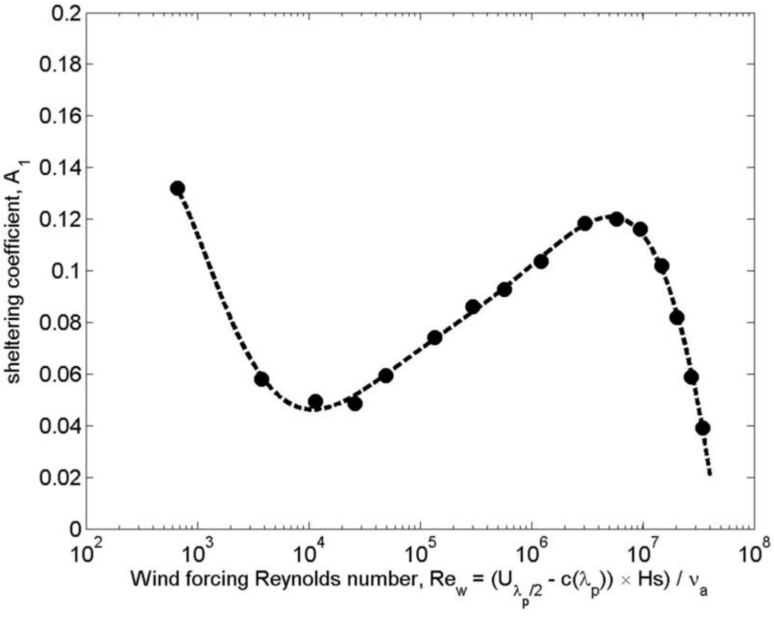

Figure 5. Sheltering coefficient versus Reynolds number from ocean measurements compared with model calculations (Figure 4). The dashed line is the fitted polynomial, equation (13).

230 km is typical of open ocean moderate wind speed observations, as may be deduced from equation (11) and the u_*/c_p estimates in Edson et al. (2013). Note that these fetch laws, equations (11) and (12), were derived using data with $U_{10} < 20$ m/s. Their accuracy at high winds is unknown. However, the fetch dependencies of both Hs and λ_p are weak, respectively $X^{0.38}$ and $X^{0.46}$ and, in addition, $U_{\lambda_p/2}-c(\lambda_p)$ changes very little for small variations in T_p. Thus the calculations of Re_w may be reasonably accurate – this is checked in section 5 using the wave model, UMWM_wideband (Appendix A) with A_1 from equation (13) below.

Here again, as for the laboratory data in section 2, the sheltering coefficient has three ranges reminiscent of flow past a circular cylinder: first decreasing as the laminar boundary layer thins for a decade increase in Re_w; then increasing as the waves steepen for two and a half decades in Re_w– here the separation of the airflow from the crests of the dominant waves is intermittent, and less so with increasing Re_w; the third regime or Reynolds number range $10^7 < \mathrm{Re}_w < 4\times10^7$, characterized by a sudden drop in the sheltering coefficient, corresponds to fully separated flow from the crests of the dominant waves – most of which are breaking. No reliable drag coefficient estimates exist at wind speeds greater than 50 m/s but, unlike the flow past a solid cylinder, no change in the flow pattern is expected as the flow skips from crest to crest and the relationship between height and length of these breaking dominant waves is a constant. Thus the sheltering coefficient is inferred to remain at its low value at $\mathrm{Re}_w=4\times10^7$ for greater Reynolds numbers. The deduced sheltering coefficients, A_1 (Figure 5) are well described with the least squares fitted seventh order polynomial in the natural logarithm of Re_w (dashed line in Figure 5). The polynomial in $x=\ln(\mathrm{Re}_w)$ with very low and very high Re_w constant tails is:

$$\begin{aligned}
&A_1=0.1318; \qquad 0 < \mathrm{Re}_w < 662\\
&A_1=8.0828\times10^{-7}x^7-7.2245\times10^{-5}x^6+2.6968\times10^{-3}x^5-5.4505\times10^{-2}x^4\\
&\quad+6.4342\times10^{-1}x^3-4.423x^2+16.3179x-24.702; \qquad 662 \le \mathrm{Re}_w \le 4\times10^7\\
&A_1=0.02077; \qquad 4\times10^7 < \mathrm{Re}_w
\end{aligned} \tag{13}$$

The drag coefficients may be calculated using equation (13) in the wave and wind stress model (UMWM_wideband). They are clearly wind and fetch (Reynolds number) dependent and are graphed in Figure 6 for fetches of 230 km and 50 km. The latter is a typical fetch of the maximum winds in hurricanes. Holland et al. (2010) give 20 km as the radius of maximum winds for a "baseline hurricane." The effective straight fetch is no more than half the circumference or 63 km.

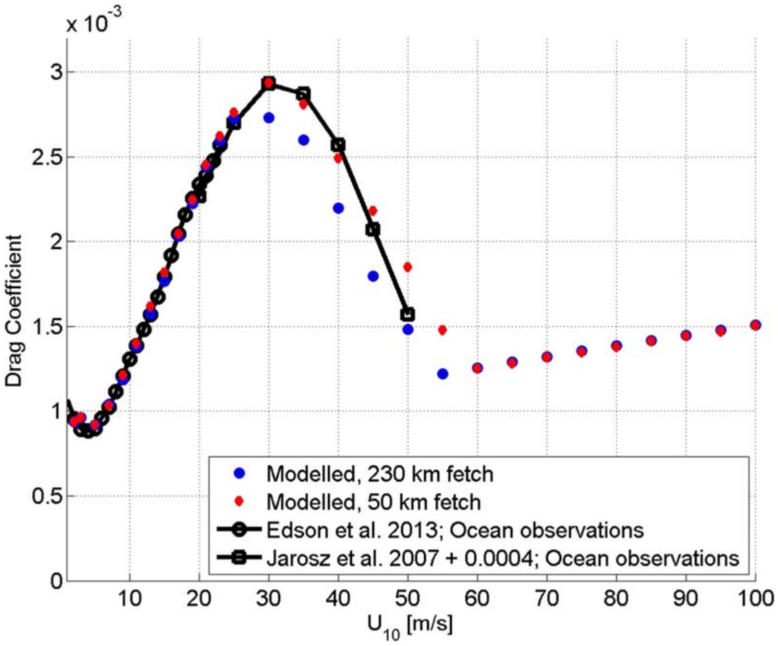

Figure 6. Modeled (with Reynolds number dependent sheltering coefficient, Figure 5, equation (13)) and observed drag coefficients versus wind speed. Note the fetch dependence of the modeled drag coefficient between 30 and 55 m/s.

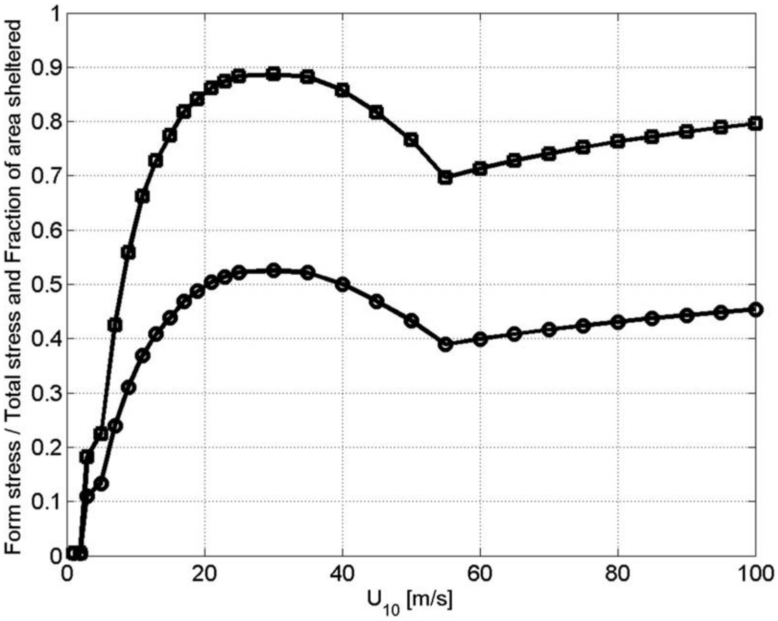

Figure 7. Form stress/total stress ratio and fraction sheltered area versus U_{10} at 230 km fetch: form stress – squares; sheltered area – circles.

The ratio of form stress to total stress and the fraction of surface sheltered (at 230 km fetch) are shown in Figure 7 versus the wind speed. The form stress rises from zero to 50% of total stress at about 8 m/s; and reaches almost 90% at U_{10} of 30 m/s; thence decreases to 70% at 55 m/s and slowly increases to 80% at 100 m/s. The sheltered area $(1-\frac{Cd'_s}{Cd_s})$ mirrors this behaviour as prescribed by equation (8). In the next section we explore the expected intensification of hurricanes governed by the drag coefficients arising from the Reynolds number dependent sheltering coefficient.

4. Maximum Winds

Emanuel (1995), in a model study of intense tropical cyclones, concluded that intensity is directly proportional to the ratio of exchange coefficients: enthalpy, *Cj*/drag, *Cd*. Intense storms are unlikely if $Cj/Cd < 0.75$. *Cj* has been shown to be roughly constant above 10 m/s at 0.0012 (Bell et al. 2012; Jeong et al. 2012) and so *Cd* must be less than 0.0016 at high winds. Indeed, the inferred *Cd* (section 3) is as low as 0.0012 at wind speed of 55 m/s, and rises slowly to 0.0016 at about 120 m/s.

Tropical cyclones gain energy from the warm surface waters and lose energy through friction in the air-sea boundary layer. The rate of heat energy input (power) at the air-sea interface or enthalpy flux is W_{in}, given by:

$$W_{in}=\rho_a CjU_{10}(j_s-j_{10});\quad [\text{watts/m}^2] \tag{14}$$

where *Cj* is the bulk enthalpy transfer coefficient and *j* is the enthalpy (j_s its surface value and j_{10} its value at 10 m height) defined:

$$j=(1-q)c_pT+q(L_v+c_{p_v}T) \tag{15}$$

Where *q* is the specific humidity, c_p is the specific heat of air, *T* is the air temperature, L_v is the latent heat of vaporization of water, and c_{p_v} is the specific heat of water vapor. W_{in} is largely a function of the sea surface temperature and the wind speed, while the frictional losses are proportional to the stress times the wind speed: $W_{out}=\rho_a C_d U_{10}^3$ (watts/m^2). Balancing the heat input (including dissipation of kinetic energy in the boundary layer), converted in a Carnot cycle to mechanical energy out, against mechanical energy lost in friction, we have:

$$\frac{T_s-T_o}{T_s}(W_{in}+W_{out})=W_{out} \tag{16}$$

where $T_s[K]=SST[^oC]+273.15$; *SST* is sea surface temperature, and T_o the stratospheric outflow temperature, taken here to be 200 K.

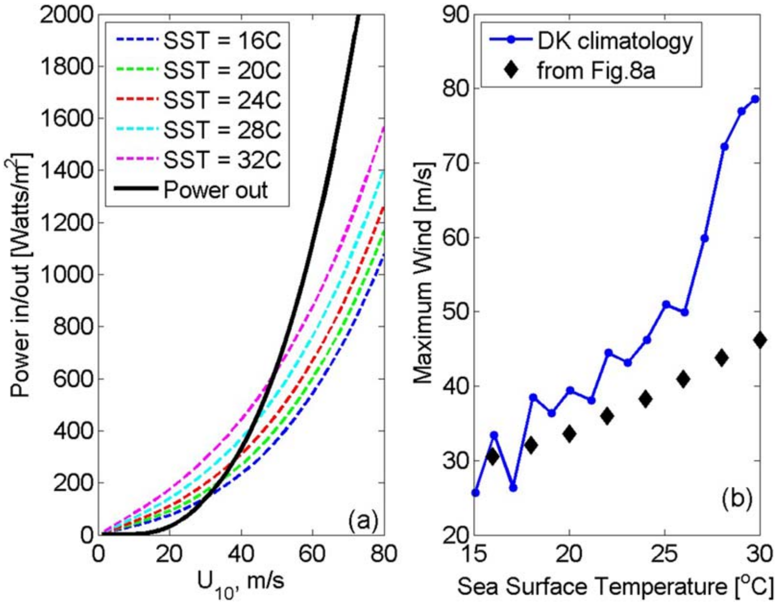

Figure 8. (a) Heat input from surface for various sea surface temperatures (SST: dashed lines) compared to frictional loss through surface drag using a constant drag coefficient above 30 m/s; (b) Climatology of maximum winds versus SST compiled by *DeMaria and Kaplan* [1994] (DK) compared to the maximum winds obtained from the intersection of dashed and solid lines in panel (a).

Both sides of equation (16) are functions of U_{10} and the balance yields the maximum expected wind speed. This balance is graphed in Figures 8a and 9a where the bulk enthalpy transfer coefficient is taken to be 0.0012 (Bell et al. 2012*;* Jeong et al. 2012), the air temperature is 1°C cooler than the sea surface temperature (SST) and the relative humidity at 10 m is 88%. The dashed lines indicate the LHS of equation (16) for different SSTs, while the solid black line in Figure 8a is the RHS of equation (16) with *Cd* as in Figure 6 (at 50 km

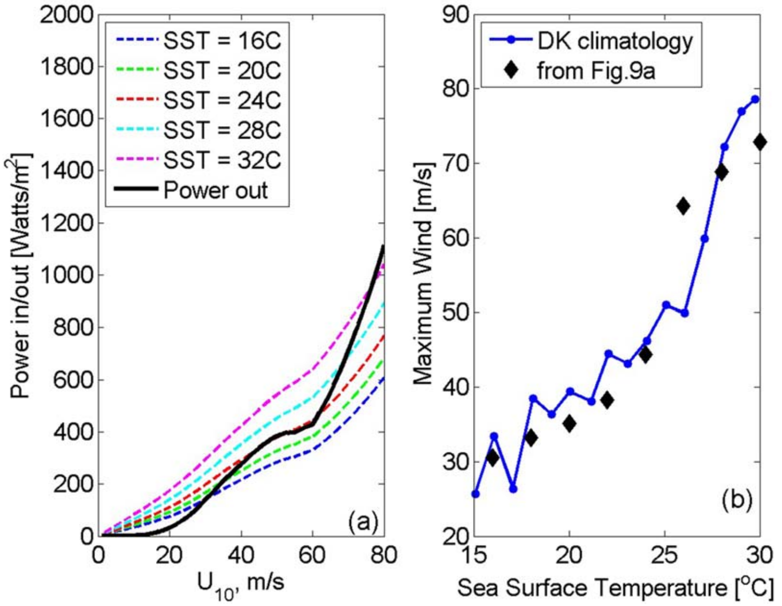

Figure 9. (a) Heat input from surface for various sea surface temperatures (SST: dashed lines) compared to frictional loss through surface drag using equation (13); decreasing drag coefficient above 30 m/s; (b) Climatology of maximum winds versus SST compiled by *DeMaria and Kaplan* [1994] (DK) compared to the maximum winds obtained from the intersection of dashed and solid lines in panel (a).

fetch) except held constant at 0.0029 above 30 m/s. In Figure 9a the solid black line indicates the RHS of equation (16) with Cd as modeled in section 3 (Figure 6 at 50 km fetch). The intersections of the solid and dashed lines yield the maximum winds for various SST values. These points are transferred to Figures 8b and 9b (black diamonds) and compared with the climatology of Atlantic tropical cyclones (1962–1988) compiled by DeMaria and Kaplan (1994) (DK). In Figure 8b, for a constant Cd for $U_{10} > 30$ m/s, the maximum winds increase slowly with SST, showing no sign of the rapid intensification at SST of 26°C that is the dominant feature of the climatology. By contrast in Figure 9b, for Cd decreasing for $U_{10} > 30$ m/s (Figure 6 at 50 km fetch), the correspondence is striking, in particular the sharp change in slope at 26°C and 50 m/s. This feature is clearly due to the pronounced decrease in the drag coefficient above 30 m/s and thus indirectly supports the field observations of drag coefficients at high winds.

5. Summary and Discussion

Laboratory measurements of waves and wind stress in increasing U_{10} yield drag coefficients that first decrease, then increase from 3 to 30 m/s and finally saturate above 30 m/s. By comparing the estimated form (wave) drag coefficient to that calculated via the measured wave spectra, the sheltering coefficient is shown to be Reynolds number dependent. The saturated drag coefficient above 30 m/s is associated with the sharp decrease in the sheltering coefficient – reminiscent of separated flow past a circular cylinder. To interpret laboratory results to the open ocean, field estimates of the drag coefficient in the range of 1 to 50 m/s are compared to those calculated in a wide band wave and wind stress model with a constant sheltering coefficient. The resulting sheltering coefficients behave in a similar fashion to the laboratory-derived sheltering coefficients, except that the sharp decrease above 30 m/s corresponds to a decreasing, rather than saturated, drag coefficient. One important consequence in modeling air-sea interactions is that the drag coefficient is a function of the dimensionless numbers, Reynolds number and wave age rather than simply wind speed as is often assumed.

Tropical cyclones provide the only natural test-beds for verifying the high wind behaviour of the aerodynamic drag coefficient. The 27-year Atlantic hurricane climatology reveals maximum winds intensifying with sea surface temperature, and rapid intensification at around 26°C. The Reynolds number dependent drag coefficients yield rapid intensification; while the constant above 30 m/s drag coefficients do not. This is an effective integral reality check of the decreasing drag coefficient in high winds. Coupled (with waves) hurricane models that employ the Reynolds number dependent sheltering coefficient, equation (13) are likely to see marked improvements in predicting intensification and decay of tropical cyclones.

The idea of a sheltering coefficient is intimately associated with the likelihood of flow separation at the crest of a wave. Following Donelan et al. (2006) separation occurs when the centripetal acceleration, a_c––required to keep the air-flow attached to the surface downstream of the crest––exceeds the downward vertical acceleration of the wave-induced flow at the crest, a_f:

$$-a_f = g + 0.5\left(U_{\lambda/2} - c(\lambda)\right)^2 (ak)^2 k \tag{17}$$

$$a_c = (U_{0.1} - c(\lambda))^2 \frac{\partial^2 \eta}{\partial x^2} \tag{18}$$

where a is the amplitude of the wave and k its wavenumber; $U_{0.1}$ is the wind speed near (10 cm above) the surface; $\frac{\partial^2 \eta}{\partial x^2}$ is the curvature of the surface. With increasing wind the wave slopes increase and the curvature increases much more rapidly. For the Stokes expansion to fourth order in slope, ak (Kinsman, 1965), the curvature at the crest is given by:

$$\frac{\partial^2 \eta}{\partial x^2} = -ak^2 \left[1 + 2ak + \frac{27}{8}(ak)^2 + \frac{49}{6}(ak)^3 + O(ak)^4\right] \tag{19}$$

The total mean square slope, $S = \overline{(\nabla \eta)^2}$ may be computed with the all wave model, UMWM_wideband (Appendix A). This is graphed in Figure 10 with the classic field observations of Cox and Munk (1954) and the laboratory measurements of Donelan and Plant (2009). S increases with U_{10} linearly at first (3 to 10 m/s) and then roughly as the square root of the wind speed. It is very weakly dependent on fetch, up to 30 m/s wind speed, as indicated by the calculations and observations at various fetches (230 km, 4 km and 14.3 m

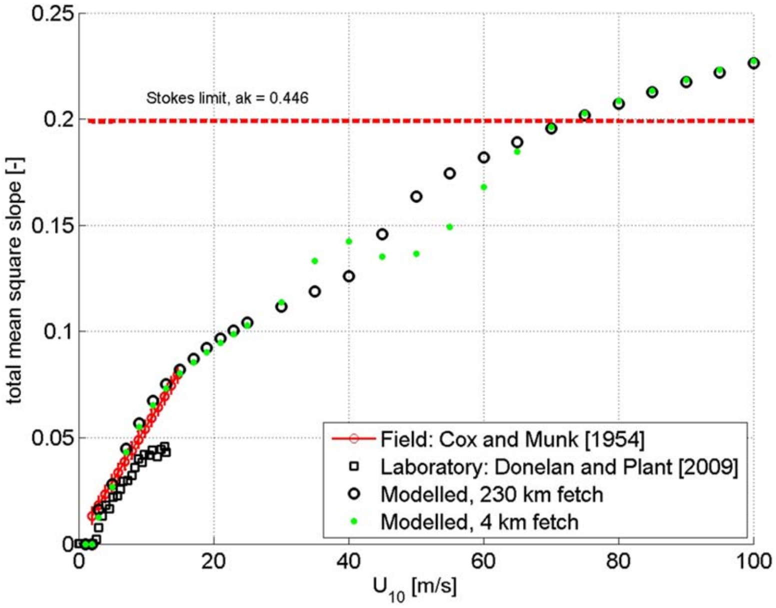

Figure 10. Measured and modeled mean square slopes versus wind speed from 1 to 100 m/s

in the laboratory). Note that the laboratory measurements saturate above 10 m/s because of the depth of the tank, which was 0.225 m. Above a wind speed of 75 m/s, the total mean square slope exceeds the Stokes breaking limit. This is due to the contribution from capillary-gravity waves, whose breaking limit slopes can be up to five times greater (Appendix A).

The amplitude of the slope of the dominant (spectral peak) waves, $ak_p=\sqrt{2S}$, is evaluated at 230 km fetch, and the competing vertical accelerations from equations (17–19) are shown in Figure 11. Above 56.15 m/s $-a_c$ exceeds $-a_f$ on all waves and the airflow separates from the crests – breaking or not – and the drag coefficient is close to its minimum value corresponding to general steady flow separation: regime 3.

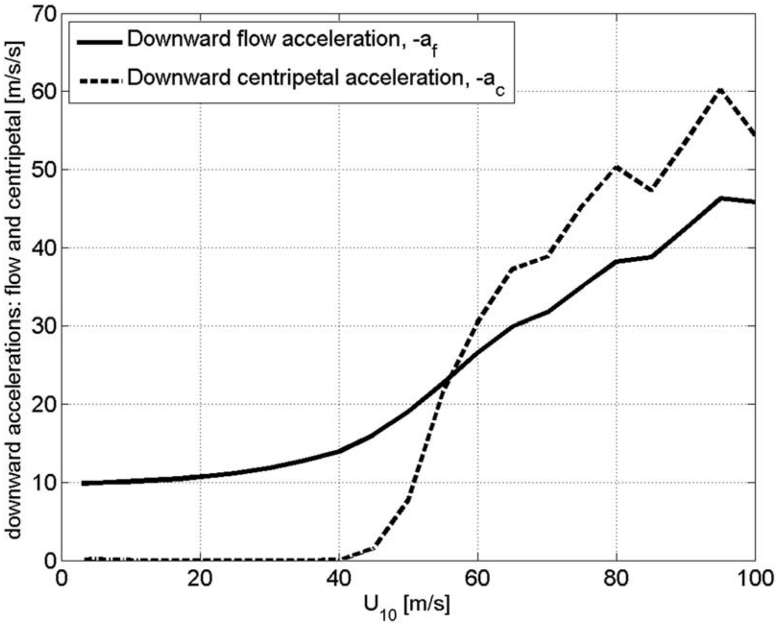

Figure 11. Competing downward accelerations at crest: the solid line is the vertical acceleration of the flow, $-a_f$, equation (17); the dashed line is the centripetal acceleration required for the flow to remain attached, $-a_c$, equations (18) and (19).

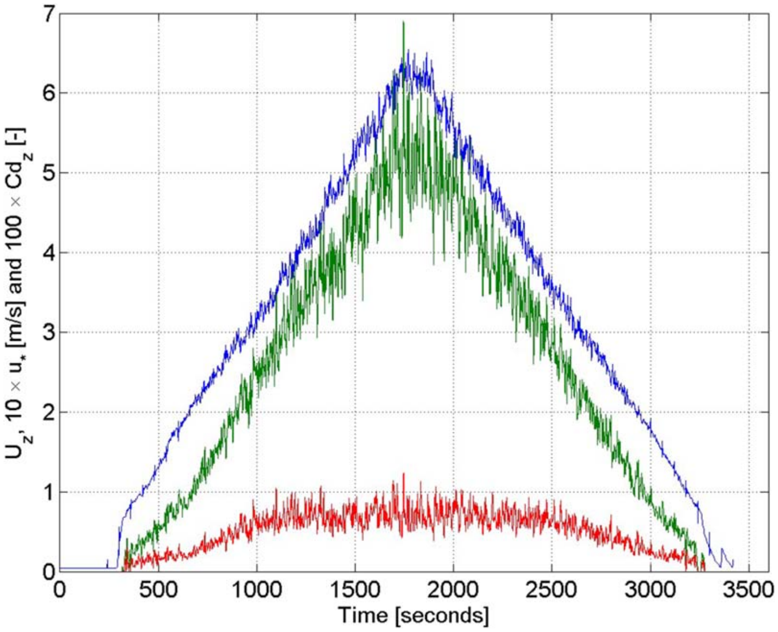

Figure A1. The forcing of the waves: U_z (blue) is the measured wind speed at height $z = 6.2$ cm; amplified friction velocity, $10 \times u_*$ (green); drag coefficient, $100 \times Cd_z$ (red).

Here the air streams from crest to crest avoiding contact with the troughs, so that aerodynamically the surface is considerably less rough than its geometric roughness, *S*. Of course, breakers and micro-breakers occur more or less intermittently at all wind speeds greater than 2.5 m/s and, having arbitrarily large curvatures downstream of the crest, induce intermittent flow separation and enhance the sheltering coefficient: regime 2. The transition from regime 2 to regime 3 appears to occur at about 30 m/s in air-sea boundary layers.

Appendix A: UMWM_Wideband

Modeling of gravity, capillary-gravity and capillary waves is required to estimate mean square slope, form drag and radar scattering from the surface. The spectra of capillary-gravity waves ($\lambda < 10$ cm, being generally in deep water), can be treated as a balance between input from the wind and dissipation due to nonlinearity and breaking (Donelan & Pierson, 1987). In a laboratory wind-wave tank, the momentum input to the waves (form stress)

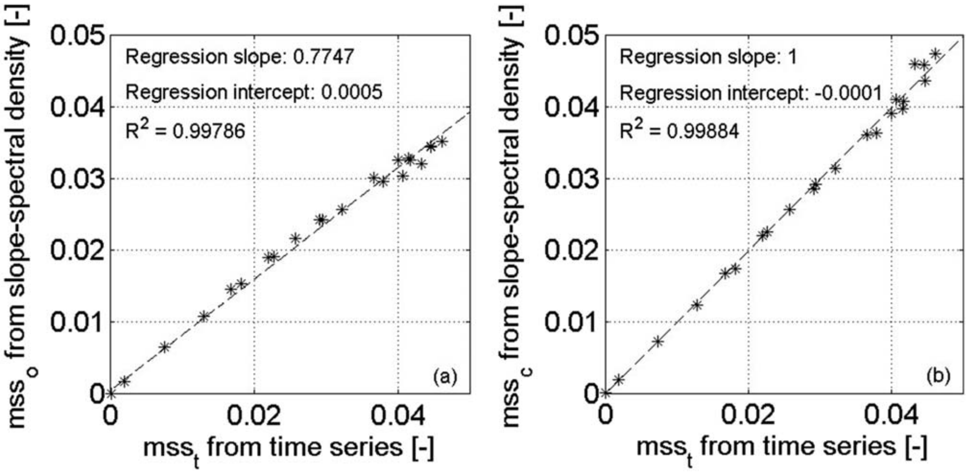

Figure A2. Comparison of mean square slope from the integral of the slope spectrum with that calculated from the slope time series: (a) – mss_o from observed wavenumbers; (b) – mss_c from corrected wavenumbers.

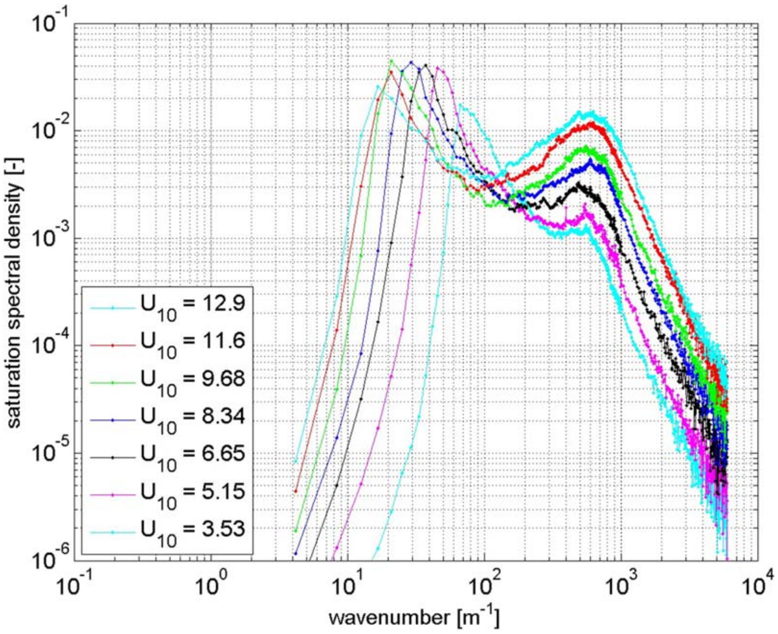

Figure A3. Saturation spectra, $B(k,\phi)=k^4E(k,\phi)$ for various wind speeds referred to 10 m height, U_{10}.

can be estimated from measurement of the total stress and the skin (viscous) stress. The measured wavenumber-directional spectrum, $E(k,\phi)$ and a model for the wind input, $S_{in}(k,\phi)$, equation (1) determine the distribution of form stress across the spectrum, $S_{in}(k,\phi)/c(k)$. Equating S_{in} and the total dissipation (viscid, S_{dv} and inviscid, S_{ds}), over a range of wind speeds, yields the parameters of the inviscid dissipation, S_{ds}; since the viscid dissipation is known theoretically ($S_{dv}=4\nu k^2E(k,\phi)$) and verified experimentally (Donelan & Plant, 2009).

Such an experiment has been conducted in which the total stress and wind speed were measured with x-film anemometry and the surface elevation and 2D slope were measured at the same point with a laser beam, linescan camera and 2D slope gauge. The details are given in Donelan and Plant (2009); it suffices to

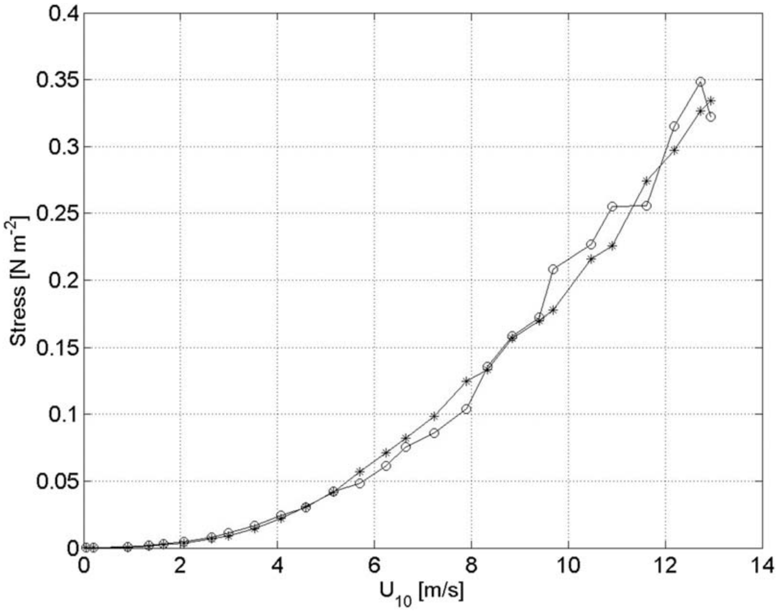

Figure A4. Stress versus wind speed referred to 10 m height: stress from measured wind velocity fluctuations – asterisks; stress from $S_{in}(k,\phi)/c(k)$ with $A_1=0.23$ – circles.

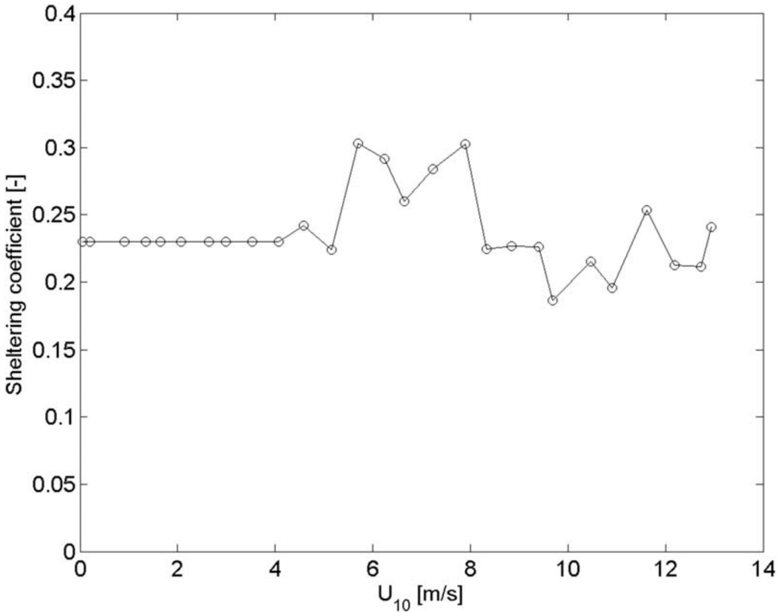

Figure A5. Sheltering coefficient determined by matching calculated form drag to measured form drag.

mention that the data were sampled at 1,000 Hz and wavelengths greater than 1 mm were resolved. The experiment was conducted with air and water temperatures at 22°C and the fan-driven wind speed increased steadily from 0 to 6 m/s (at 6.2 cm above still water level) and back to zero at the same rate over 1 hour. One second averages of the wind speed, friction velocity and resultant drag coefficient are shown in Figure A1. The data analyzed herein were 28 one minute (60,000 samples) sets from 180 s to 1,800 s; i.e., the rising arm of the ramp with U_{10} increasing from 0.05 m/s to 12.93 m/s.

The wavenumber-directional spectrum, $E(k, \phi)$ is obtained with the Wavelet Directional Method (WDM) (Donelan et al., 1996). Wavenumbers are resolved in frequency bins through the phase differences among

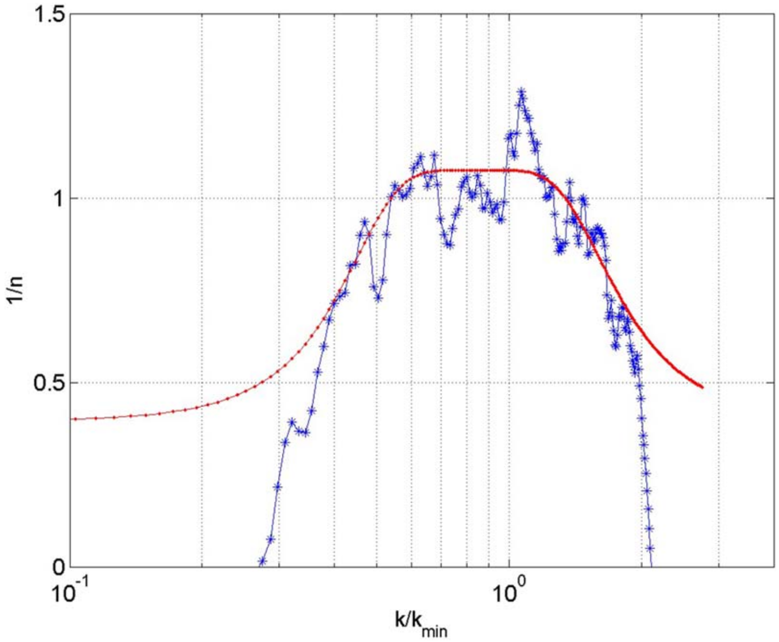

Figure A6. The inverse of the power of the saturation spectrum in the dissipation function versus normalized wavenumber: calculation from tank measurements – blue asterisks; fitted curve, equation (A4) – red dots.

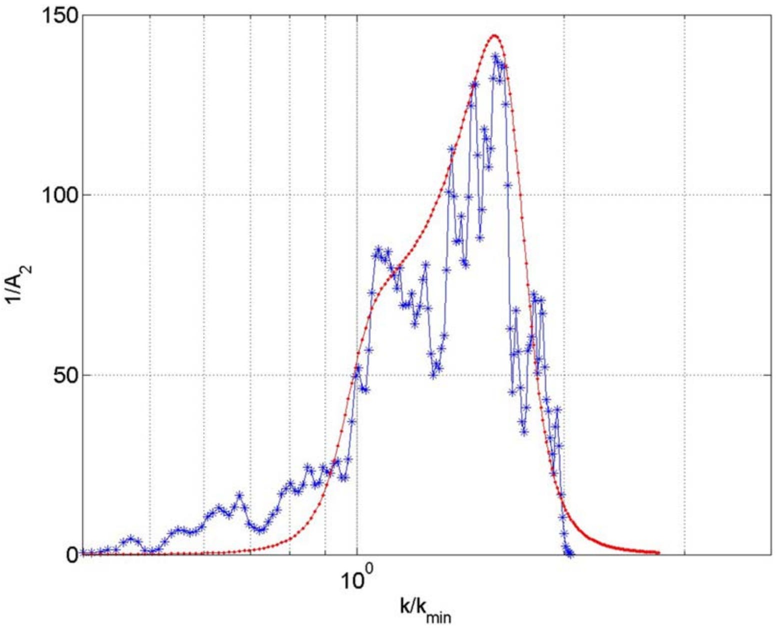

Figure A7. The inverse of the multiplier of the saturation spectrum in the dissipation function versus normalized wavenumber: calculation from tank measurements – blue asterisks; fitted curve, equation (A5) – red dots.

virtual wave staffs (a square quartet derived from the elevation and slope gauges) at every sample point. The Doppler shifting of the frequencies, due to the drift current, u_z, produces a general reduction in the observed magnitude of the wavenumber, k_o. This is apparent in the comparison of the mean square slope (*mss*) derived from the integral of the wavenumber spectrum, ($mss_o = \int_{-\pi}^{\pi} \int_{0}^{6000} k_o^2 E(k_o, \phi) k_o dk_o d\phi$), with mss_t derived from the time series of slopes (Figure A2a).

The regression slope (0.7747) corresponds to a wind drift correction of about 14% of phase velocity, $c(k_o)$. The correction required is $k = k_o(1 + u_{-1/k_o} \cos \phi / c(k_o))$ and when applied with a logarithmically decreasing wind drift at $z = -1/k_o$ a nearly perfect fit of mss_c with mss_t is achieved with drift current given by:

$$u_{-1/k_o} = \sqrt{\frac{\rho_a}{\rho_w}} \frac{u_*}{\kappa} \ln (0.4895Dk) \tag{A1}$$

where D is the depth of water in the tank (0.225 m) and the return drift starts at a depth of 0.4895, $D = 11$ cm.

The observed amplitudes are binned by observed direction and corrected wavenumber to yield the wavenumber-directional spectrum. To examine the wind sensitivity the saturation spectra ($B(k, \phi) = k^4 E(k, \phi)$) for various wind speeds are plotted in Figure A3.

The wind sensitivity is greatest in the capillary-gravity range ($200 < k < 1{,}000$ m^{-1}); being about U^2. Whereas in the gravity wave equilibrium range it is about $U^{0.3}$. The equilibrium range parameter, α is the level of the saturation spectrum from $2k_p$ to $10k_p$; where k_p is the wavenumber at the peak of the spectrum. In these laboratory spectra the equilibrium range is very narrow and thus the wind sensitivity there is difficult to discern. However, the analysis of field data by Donelan et al. (1985) found that $\alpha \propto \left(\frac{U_{10}}{c_p}\right)^{0.55}$ and $c_p \propto U_{10}^{0.54}$ so that the wind sensitivity in the gravity wave equilibrium range is $U_{10}^{0.253}$, about eight times less sensitive than the capillary-gravity waves.

The sheltering coefficient, A_1 (equation (1)) may be obtained, as in section 2, by comparing the computed form drag coefficient (with A_1 set to 0.23) plus the sheltering attenuated skin drag coefficient to the measured total drag coefficient (Figure A4).

The actual A_1 values are obtained as in section 2, equation (5), and shown in Figure A5. The sheltering coefficient does not change significantly over the U_{10} range of 4 to 13 m/s, yet the capillary-gravity waves are highly wind sensitive and the gravity waves are not. The explanation given by Donelan and Pierson (1987) rests on the variation of dispersity with wavenumber. Essentially the dispersive gravity waves steepen and break largely through the interaction of groups (constructive interference), whereas the non-dispersive capillary-gravity waves near the wavenumber of minimum phase speed ($k_{\min}=\sqrt{\frac{g\rho_w}{\gamma}}$) do not form groups and hence break at a higher average slope. This all-wave behaviour can be incorporated in the inviscid dissipation function as suggested by Donelan and Pierson (1987) and later expanded (Donelan et al., 2012) to include modulation of the short waves by long wave slopes:

$$S_{ds}=-A_2\left[1+A_3\chi^2(k,\phi)\right]^2[B(k,\phi)]^n\omega(k)E(k,\phi) \tag{A2}$$

where A_2 and n are functions of $k/k_{\min}$ and χ^2 is the mean square slope in the direction, ϕ of all waves longer than $\lambda(k)$. A_3 was determined by laboratory experiment in which long paddle-generated waves were added to wind-generated waves (Donelan et al., 2010); $A_3=240$. The values of n and A_2 for gravity waves were set to 2.53 and 46.665 by comparison with data from the North Sea (Donelan et al., 2012).

The increased wind sensitivity in the capillary-gravity region implies much reduced n and A_2 there. Equating input and dissipation in the wind direction (ϕ=0), we have:

$$\frac{S_{in}(k,0)-S_{dv}(k,0)}{(1+240\chi^2)^2E(k,0)}=A_2(k)\left[k^4E(k,0)\right]^{n(k)}\omega(k) \tag{A3}$$

From which $n(k)$ and $A_2(k)$ are readily found by least-squares regression of $\ln(E(k,0))$ against ln(LHS) for $U_{10}>8$ m/s. Their inverses are graphed in Figures A6 and A7.

$n(k)$ and $A_2(k)$ are fitted with the following expressions (shown in red), in which the reduced regions are centered on $k_n=0.85k_{\min}$ and $k_A=1.32k_{\min}$ respectively.

$$n(k)=1.6\left|2-\frac{1+3(k/k_n)^3}{1+(k/k_n)^3}\right|^6+0.93 \tag{A4}$$

$$A_2(k)=46.65\left|2-\frac{1+3(k/k_A)^2}{1+(k/k_A)^2}\right|^7+0.01+0.0045\ \tanh(0.01(k_A-k)) \tag{A5}$$

The shifts away from $k_{\min}$ of $n(k)$ and $A_2(k)$ and the asymmetry of $A_2(k)$ about k_A are due to the difference in breaking steepness of gravity waves and capillary waves. The breaking limit, H_B/λ is 0.142 for gravity waves and 0.73 for purely capillary waves (Kinsman, 1965). The inviscid dissipation sink function, S_{ds} permits the modeling of all waves – gravity, capillary-gravity and capillary – with the UMWM_wideband model.

Acknowledgments
I acknowledge fruitful discussions with A. Babanin, M. Banner, G. Mellor, A. Soloviev, Q. Song, I. Young and Z-K. Zhao. The data used in this paper are stored in Matlab form in the supporting information.

References

Batchelor, G. K. (1967). *An introduction to fluid dynamics*. Cambridge, UK: Cambridge University Press.

Bell, M. M., Montgomery, M. T., & Emanuel, K. A. (2012). Air–sea enthalpy and momentum exchange at major hurricane wind speeds observed during CBLAST. *Journal of the Atmospheric Sciences*, *69*(11), 3197–3222. https://doi.org/10.1175/jas-d-11-0276.1

Cox, C. S., & Munk, W. H. (1954). Measurements of the roughness of the sea surface from photographs of the sun's glitter. *Journal of Optical Society of America*, *44*, 838–850.

DeMaria, M., & Kaplan, J. (1994). A Statistical Hurricane Intensity Prediction Scheme (SHIPS) for the Atlantic Basin. *Weather and Forecasting*, *9*(2), 209–220. https://doi.org/10.1175/1520-0434(1994)009<0209:ASHIPS>2.0.CO;2

Donelan, M., Hamilton, J., & Hui, W. H. (1985). Directional spectra of wind-generated waves. *Philosphical Transactions of Royal Society of London A: Mathematical, Physical, and Engineering Sciences*, *315*, 509–562.

Donelan, M. A. (1978). Whitecaps and momentum transfer. In A. Favre, & K. Hasselmann (Eds.), *Turbulent fluxes through the sea surface, wave dynamics & prediction* (pp. 273–287). New York, NY: Plenum.

Donelan, M. A., Drennan, W. M., & Magnusson, A. K. (1996). Non-stationary analysis of the directional properties of propagating waves. *Journal of Physical Oceanography*, *26*, 1901–1914.

Donelan, M. A. (1999). Wind-induced growth and attenuation of laboratory waves. In S. G. Sajjadi, N. H. Thomas, & J. C. R. Hunt (Eds.), *Wind-Over-Wave Couplings* (pp. 183–194). Oxford, UK: Oxford University Press.

Donelan, M. A. (2017). Frequency-direction spectra of wind-generated gravity waves. In J. Carlton, P. Jukes, & Y.-S. Choo (Eds.), *Encyclopedia of maritime and offshore engineering* (4320 pp.). NJ: John Wiley & Sons. https://doi.org/10.1002/9781118476406.emoe079

Donelan, M. A., Babanin, A. V., Young, I. R., & Banner, M. L. (2006). Wave-follower field measurements of the wind-input spectral function. Part II: Parameterization of the wind input. *Journal of Physical Oceanography*, *36*, 1672–1689.

Donelan, M. A., Curcic, M., Chen, S. S., & Magnusson, A. K. (2012). Modeling waves and wind stress. *Journal of Geophysical Research*, *117*, C00J23. https://doi.org/10.1029/2011JC007787

Donelan, M. A., Haus, B. K., Plant, W. J., & Troianowski, O. (2010). Modulation of short wind waves by long waves. *Journal of Geophysical Research*, *115*, C10003. https://doi.org/10.1029/2009JC005794

Donelan, M. A., Haus, B. K., Reul, N., Plant, W. J., Stiassnie, M., Graber, H. C., et al. (2004). On the limiting aerodynamic roughness of the ocean in very strong winds. *Geophysical Research Letters*, *31*(18), L18306. https://doi.org/10.1029/2004GL019460

Donelan, M. A., & Pierson, W. J. (1987). Radar scattering and equilibrium ranges in wind-generated waves with application to scatterometry. *Journal of Geophysical Research*, *93*, 4871–5029.

Donelan, M. A., & Plant, W. J. (2009). A threshold for wind-wave growth. *Journal of Geophysical Research*, *114*, C07012. https://doi.org/10.1029/2008JC005238

Edson, J. B., Jampana, V., Weller, R. A., Bigorre, S. P., Plueddemann, A. J., Fairall, C. W., et al. (2013). On the exchange of momentum over the open ocean. *Journal of Physical Oceanography*, *43*(8), 1589–1610. https://doi.org/10.1175/jpo-d-12-0173.1

Emanuel, K. A. (1995). Sensitivity of tropical cyclones to surface exchange coefficients and a revised steady-state model incorporating eye dynamics. *Journal of Atmospheric Sciemces*, *52*, 3969–3976.

Grare, L., Peirson, W. L., Branger, H., Walker, J. W., Giovanangeli, J.-P., & Makin, V. (2013). Growth and dissipation of wind-forced, deep-water waves. *Journal of Fluid Mechanics*, *722*, 5–50. https://doi.org/10.1017/jfm.2013.88

Golbraikh, E., & Shtemler, Y. M. (2016). Foam input into the drag coefficient in hurricane conditions. *Dynamics of Atmospheres and Oceans*, *73*, 1–9.

Holland, G. J., Belanger, J. I., & Fritz, A. (2010). A revised model for radial profiles of hurricane winds. *Monthly Weather Review*, *138*, 4393–4401.

Holthuijsen, L. H., Powell, M. D., & Pietrzak, J. D. (2012). Wind and waves in extreme hurricanes. *Journal of Geophysical Research*, *117*, C09003. https://doi.org/10.1029/2012JC007983

Hsiao, S. V., & Shemdin, O. H. (1983). Measurements of wind velocity and pressure with a wave follower during MARSEN. *Journal of Geophysical Research*, *88*, 9841–9849.

Jarosz, E., Mitchell, D. A., Wang, D. W., & Teague, W. J. (2007). Bottom-up determination of air-sea momentum exchange under a major tropical cyclone. *Science*, *315*(5819), 1707–1709. https://doi.org/10.1126/science.1136466

Jeffreys, H. (1924). On the formation of waves by wind. *Proceedings of Royal Society of London, Series A*, *107*, 189–206.

Jeffreys, H. (1925). On the formation of waves by wind. *Proceedings of Royal Society of London, Series A*, *110*, 341–347.

Jeong, D., Haus, B. K., & Donelan, M. A. (2012). Enthalpy transfer across the air–water interface in high winds including spray. *Journal of the Atmospheric Sciences*, *69*(9), 2733–2748. https://doi.org/10.1175/JAS-D-11-0260.1

Kinsman, B. (1965). *Wind waves; their generation and propagation on the ocean surface* (676 pp.). Englewood Cliffs, NJ: Prentice-Hall Inc.

Kudryavtsev, V. N., & Makin, V. K. (2007). Aerodynamic roughness of the sea surface at high winds. *Boundary Layer Meteorology*, *125*, 289–303. https://doi.org/10.1007/s10546-007-9184-7

Kukulka, T., Hara, T., & Belcher, S. E. (2007). A model of the air-sea momentum flux and breaking-wave distribution for strongly forced wind waves. *Journal of Physical Oceanography*, *37*(7), 1811–1828. https://doi.org/10.1175/JPO3084.1

Makin, V. K. (2005). A note on drag of the sea surface at hurricane winds. *Boundary Layer Meteorology*, *115*(1), 169–176. https://doi.org/10.1007/s10546-004-3647-x

Miles, J. W. (1957). On the generation of surface waves by shear flows. *Journal of Fluid Mechanics*, *3*, 185–204. https://doi.org/10.1017/S0022112057000567

Phillips, O. M. (1977). *The dynamics of the upper ocean* (336 pp.). Cambridge, UK: Cambridge University Press.

Powell, M. D., Vickery, P. J., & Reinhold, T. A. (2003). Reduced drag coefficient for high wind speeds in tropical cyclones. *Nature*, *422*(6929), 279–283. https://doi.org/10.1038/nature01481

Reul, N. (1998). *Etude expérimentale de la structure de l'écoulement d'air au-dessus de vagues courtes déferlantes* (Ph.D. thesis, 334 pp.). Marseille, France: Univ. de la Mediterranee.

Soloviev, A. V., Lukas, R., Donelan, M. A., Haus, B. K., & Ginis, I. (2014). The air–sea interface and surface stress under tropical cyclones. *Scientific Reports*, *4*, 5306. https://doi.org/10.1038/srep05306

Takagaki, N., Komori, S., Suzuki, N., Iwano, K., Kuramoto, T., Shimada, S., et al. (2012). Strong correlation between the drag coefficient and the shape of the wind sea spectrum over a broad range of wind speeds. *Geophysical Research Letters*, *39*, L23604. https://doi.org/10.1029/2012GL053988

Takagaki, N., Komori, S., Suzuki, N., Iwano, K., & Kurose, R. (2016). Mechanism of drag coefficient saturation at strong wind speeds. *Geophysical Research Letters*, *43*, 9829–9835. https://doi.org/10.1002/2016GL070666

Troitskaya, Y. I., Sergeev, D. A., Kandaurov, A. A., Baidakov, G. A., Vdovin, M. A., & Kazakov, V. I. (2012). Laboratory and theoretical modeling of air-sea momentum transfer under severe wind conditions. *Journal of Geophysical Research*, *117*, C00J21. https://doi.org/10.1029/2011JC007778

Wu, J. (1975). Wind-induced drift currents. *Journal of Fluid Mechanics*, *68*, 49–70.

Yang, D., Meneveau, C., & Shen, L. (2013). Dynamic modelling of sea-surface roughness for large-eddy simulation of wind over ocean wavefield. *Journal of Fluid Mechanics*, *726*, 62–99.